Stretching, Coalescence, and Mixing in Porous Media

Tanguy Le Borgne*
Geosciences Rennes, UMR 6118, Université de Rennes 1, CNRS, 35042 Rennes, France

Marco Dentz
Spanish National Research Council (IDAEA-CSIC), 08034 Barcelona, Spain

Emmanuel Villermaux†
Institut de Recherche sur les Phénomènes Hors Equilibre, Aix-Marseille Université, 13384 Marseille Cedex 13, France
(Received 18 February 2013; published 13 May 2013)

We study scalar mixing in heterogeneous conductivity fields, whose structural disorder varies from weak to strong. A range of stretching regimes is observed, depending on the level of structural heterogeneity, measured by the log-conductivity field variance. We propose a unified framework to quantify the overall concentration distribution predicting its shape and rate of deformation as it progresses toward uniformity in the medium. The scalar mixture is represented by a set of stretched lamellae whose rate of diffusive smoothing is locally enhanced by kinematic stretching. Overlap between the lamellae is enforced by confinement of the scalar line support within the dispersion area. Based on these elementary processes, we derive analytical expressions for the concentration distribution, resulting from the interplay between stretching, diffusion, and random overlaps, holding for all field heterogeneities, residence times, and Péclet numbers.

DOI: 10.1103/PhysRevLett.110.204501 PACS numbers: 47.51.+a, 47.56.+r

Understanding the impact of the stirring field heterogeneity on the concentration distribution of a mixture being transported by the flow is a central question of the physics of mixing in fluids. Because of its obvious bearing on a variety of associated phenomena, such as chemical reactions, kinetics, chemotaxis, and biological activity [1–3], this question has received various kinds of answers (see, e.g., [4–6]).

We are concerned here with porous media, which, unlike fluids, have a structure which does not deform in general. However, their flow heterogeneity at different scales generates a similar folding and stretching [7,8] to those in stirred fluids. Mixing in such flows controls important subsurface processes, including the kinetics of biogeochemical reactions, the migration of contaminants, the development of biofilms, and the geological storage of carbon dioxide [9–14].

Velocity fields in soils or permeable rocks are among the most heterogeneous flows in nature, since the medium conductivity can easily vary over several orders of magnitude over short distances [15]. While many studies have investigated the upscaling of dispersive spreading, which quantifies the spatial extent of transported plumes, the upscaling of mixing and variability of concentration levels in porous media is still an open issue [8,12,16]. For some simple flow fields [17] or idealized processes [18], the concentration probability density function (PDF) has been derived analytically. However, the most common approach is to assume an *ad hoc* distribution and parametrize it from the evolution of low order concentration moments, usually invoking the assumption of weak heterogeneity [19].

From the analysis of the processes altering the mixture in a synthetic porous medium, we decipher the distinct roles played by stretching enhanced diffusion and interaction rules between nearby elements [20] to develop a unified mixing theory for heterogeneous porous media, providing an analytical prediction of the concentration PDF for arbitrary heterogeneity and Péclet numbers [21].

We consider mixing in two-dimensional heterogeneous porous media, which are characterized by a spatially variable hydraulic conductivity $K(\mathbf{x})$ (Fig. 1). The joint distribution of the point values of log-conductivity $\ln K(\mathbf{x})$ is multivariate Gaussian and characterized by the correlation length λ and a variance $\sigma^2_{\ln K}$. The correlation function of $\ln K$ fluctuations is of Gaussian shape. This type of random conductivity field is generic and represents a reference field for theories of flow and transport in heterogeneous porous media [10,15]. Spatial variability of the conductivity $K(\mathbf{x})$ is mapped onto the divergence-free flow field $\mathbf{u}(\mathbf{x})$ via the Darcy equation $\mathbf{u}(\mathbf{x}) = -K(\mathbf{x})\nabla h(\mathbf{x})$, with $h(\mathbf{x})$ the hydraulic head [see an example of a velocity field in Fig. 2(c)]. Transport of a passive scalar $c(\mathbf{x}, t)$ in the flow field $\mathbf{u}(\mathbf{x})$ is described by the Fokker-Planck or advection-diffusion equation

$$\frac{\partial c(\mathbf{x}, t)}{\partial t} + \mathbf{u}(\mathbf{x}) \cdot \nabla c(\mathbf{x}, t) - D\nabla^2 c(\mathbf{x}, t) = 0, \qquad (1)$$

where D denotes the (constant) diffusion coefficient.

As boundary conditions, we impose an instantaneous line injection at $x_0 = \lambda$ with homogeneous concentration $c_0 = 2 \times 10^{-3}$, no flux at the horizontal boundaries, and a

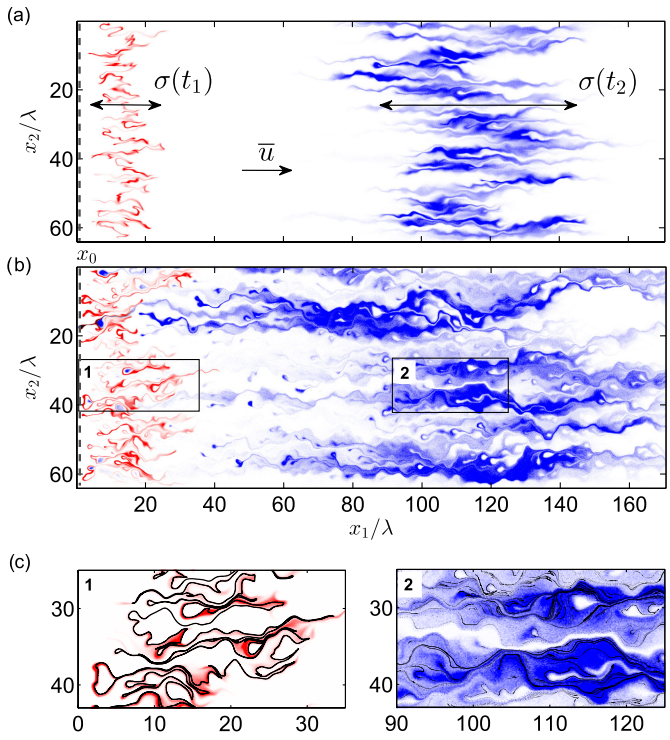

FIG. 1 (color online). Concentration field c at times $t_1 = 12.5\tau_a$ (proportional to color intensity) and $t_2 = 112.5\tau_a$ (proportional to color intensity), for an initial line injection with uniform concentration $c_0 = 2 \times 10^{-3}$ at longitudinal position $x_0 = \lambda$ (dashed black line), a Péclet number $\mathrm{Pe} = 8 \times 10^2$, and permeability field variances equal to (a) $\sigma^2_{\ln K} = 1$ and (b) $\sigma^2_{\ln K} = 4$. The plume is transported from left to right with a mean velocity $\bar{u}$ and a dispersion length $\sigma(t)$ increasing with time. (c) zoom of the concentration fields at each time with superimposition of a purely advected line (black lines), initially located at $x_0 = \lambda$, illustrating the composition of the mixture by stretching and diffusive coalescence (see also the corresponding velocity field in Fig. 2).

perfectly absorbing boundary at the outlet. The flow equation is solved numerically with a finite difference scheme over the domain $\Omega = \{\mathbf{x} | x_1 \in [0, 819.2\lambda], x_2 \in [0, 102.4\lambda]\}$. The spatial discretization scale is set as $\lambda/8$. Transport is solved by particle tracking using 10^7 particles, which provides an accurate simulation of the concentration field down to a minimum concentration of 10^{-6}. The characteristic advection time scale is defined by $\tau_a = \lambda/\bar{u}$, where $\bar{u}$ is the mean transport velocity. The characteristic diffusion time is $\tau_D = \lambda^2/D$. The Péclet number $\mathrm{Pe} = \lambda\bar{u}/D$ compares the diffusive and advective time scales.

Figure 1 displays the simulated concentration field at different times for moderate and strong heterogeneities and a Péclet number $\mathrm{Pe} = 8 \times 10^2$. The scalar line, initially located perpendicular to the main flow direction, distorts into a brush with a typical streamwise width $\sigma(t)$, increasing in time. The brush is made of a collection of strips, aligned on average with the direction of the mean flow. At early times, the scalar concentration is close to uniform along the stretching direction and varies rapidly along the compressive one [Fig. 1(c)], thus forming a lamellalike topology [22]; the concentration field can be seen as a set of lamellae, whose concentration depends on the interaction between local stretching and diffusion. Compression perpendicular to the stretching direction enhances diffusive mass transfer by steepening the scalar gradient. At later times, neighboring lamellae overlap by diffusive coalescence. The concentration field is then composed of lamella aggregates and concentration lacunarities [Fig. 1(c)]. Although the following derivations are done for the 2D case, the basic processes governing the temporal evolution of the concentration field in 3D are similar, with 2D sheets as elementary structures rather than lamellae [22,23].

The impact of stretching on the concentration distribution can be quantified by considering the elementary processes at the scale of a single lamella, of initial size L_0, width s_0, and concentration c_0. The temporal evolution of the concentration $c(\zeta, t)$ at a position ζ along the direction perpendicular to the lamella is [6,24,25]

$$c(\zeta, t) = \frac{c_0 \exp\left[-\frac{\zeta^2/s(t)^2}{1+4\tau(t)}\right]}{\sqrt{1+4\tau(t)}}, \tag{2}$$

where the expression of $\tau(t)$ depends on the temporal evolution of the lamella elongation $\rho(t) = L(t)/L_0$

$$\tau = \int_0^t dt' \frac{D\rho(t')^2}{s_0^2}. \tag{3}$$

The concentration distribution across the lamella is Gaussian, with a maximum concentration θ given by

$$\theta(\tau) = \frac{c_0}{\sqrt{1+4\tau}}. \tag{4}$$

The PDF of concentration point values that correspond to the distribution (2) with a concentration range of $[\epsilon, \theta]$ is given by

$$p_c(c|\theta) = \frac{1}{c\sqrt{\ln(\theta/\epsilon)\ln(\theta/c)}}, \tag{5}$$

where ϵ and θ are, respectively, the minimum and maximum concentrations in the strip.

In the regime where the lamellae do not overlap, the total concentration PDF can be obtained from the PDF of maximum concentrations $p_m(\theta, t)$ as

$$p_c(c, t) = \int_c^{c_0} d\theta \frac{p_m(\theta, t)}{c\sqrt{\ln(\theta/\epsilon)\ln(\theta/c)}}, \tag{6}$$

with $c \geq \epsilon$. This expression depends on the distribution of $\tau(t)$ through (4) and thus on the history of lamella elongations $\rho(t)$ through (3).

The distribution of elongations $p_\rho(\rho, t)$ at each time is quantified numerically by computing the pair separation $L(t)$ of advecting particles, originally regularly distributed

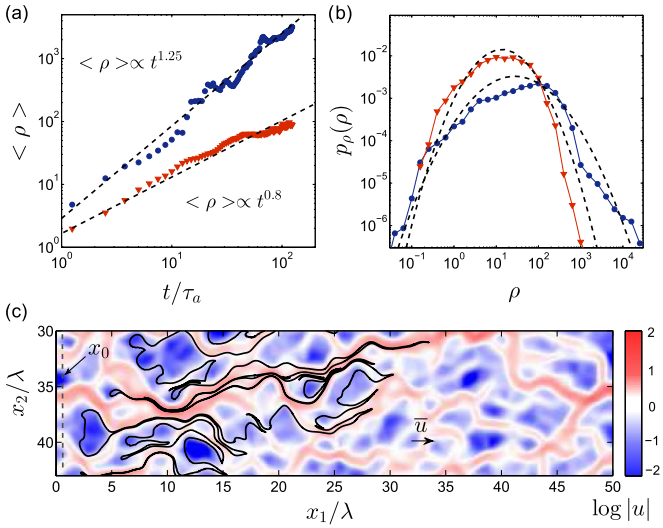

FIG. 2 (color online). (a) Temporal evolution of the average elongation $\langle\rho\rangle$ for permeability field variances $\sigma^2_{\ln K} = 1$ (red triangles) and $\sigma^2_{\ln K} = 4$ (blue disks). (b) Elongation PDF computed at time $t_2 = 112.5\tau_a$ for $\sigma^2_{\ln K} = 1$ (red triangles) and $\sigma^2_{\ln K} = 4$ (blue disks). Fitted log-normal distributions are represented as black dashed lines. (c) Zoom of the velocity field and advected line (black lines) for $\sigma^2_{\ln K} = 4$ at time $t_1 = 12.5\tau_a$.

on the injection line, with a separation distance $L_0 = 1.25 \times 10^{-4}\lambda$ [Fig. 2(c)]. The structural heterogeneity leads to a broad distribution of elongations $\rho = L/L_0$ [Fig. 2(b)], with a significant probability of values less than 1, which implies the existence of compression processes. Note that, for large elongations, particle pairs may split and take independent paths as a consequence of the finiteness of the number of particles used to estimate the pair separation. This issue can be addressed by refining the line discretization, i.e., increasing the number of particles, as the length of the line increases [25]. Here, we performed numerical tests to choose a sufficiently large initial number of particles to ensure a good quantification of the elongation statistics.

The average elongation is found to grow as

$$\langle\rho\rangle = (t/\tau_a)^\alpha, \tag{7}$$

where the exponent α ranges from $\alpha = 0.8$ for the moderate heterogeneity field to $\alpha = 1.25$ for the strong heterogeneity field [Fig. 2(a)].

The nonlinear nature of stretching has important implications for the geometry of the line. During its transport, the advected line is confined in a domain whose longitudinal extent grows as the characteristic spreading length $\sigma(t)$ and whose lateral extent is constant [Fig. 1(a)]. For the considered conductivity fields, advective spreading scales as

$$\sigma \propto t^{\beta/2}, \tag{8}$$

where β ranges from $\beta = 1$ for the moderate heterogeneity to $\beta = 1.4$ for the strong heterogeneity. The superdiffusive behavior $\beta > 1$ observed for strongly heterogenous media is expected to reflect a crossover between the initial ballistic to the ultimate diffusive dispersion regime [21], but it is generally persistent over a significant range of times [26].

The power law behavior of the mean elongation $\langle\rho(t)\rangle$ and the dispersion length $\sigma(t)$ implies that the advected line can be characterized by a fractal dimension D_f, such that

$$\langle\rho\rangle \propto \sigma^{D_f}, \tag{9}$$

where D_f is the fractal dimension of the line

$$D_f = 2\alpha/\beta. \tag{10}$$

Equation (10) provides a key relationship between deformation, spreading, and the geometry of the scalar field. The fractal dimension of the advected line support, computed by box counting, is found to be well defined over 2 orders of magnitude in space. It is independent of time and ranges from $D_f = 1.6$ for the moderate heterogeneity to $D_f = 1.8$ for the strong heterogeneity, which is consistent with Eq. (10). Based on this equation, we can estimate the upper and lower bounds for the exponent α to be $\alpha = 1/2$ for weak random heterogeneities ($\beta = 1$ and $D_f = 1$) and $\alpha = 2$ for strongly structured stratified conductivity fields ($\beta = 2$ and $D_f = 2$). Hence, the elongation temporal scaling can follow a broad range of temporal behaviors, from diffusive to quadratic.

A simple stochastic model of Lagrangian elongation, which reflects the multiplicative nature of the stretching process and satisfies the temporal power law behavior of the mean elongation (7), is the following Langevin equation

$$\frac{1}{\rho}\frac{d\rho}{dt} = \frac{\mu}{t} + \sqrt{\frac{2\nu}{t}}\xi(t), \tag{11}$$

where $\xi(t)$ is taken as a Gaussian white noise, with $\langle\xi(t)\rangle = 0$ and $\langle\xi(t)\xi(t')\rangle = \delta(t - t')$, which results from the observed short-range temporal correlation of computed Lagrangian stretching rates $(1/\rho)(d\rho/dt)$. Considering this equation in the Stratonovich interpretation [27], this multiplicative noise structure implies that $z = \ln(\rho)$ is normally distributed and that $p_\rho(\rho)$ is log-normal, in agreement with the computed elongation distributions [Fig. 2(b)]. With the initial condition $\rho(t = \tau_a) = 1$, we obtain by integration of (11)

$$\rho = (t/\tau_a)^\mu \exp\left[\int_{\tau_a}^{t} dt' \sqrt{\frac{2\nu}{t'}}\xi(t')\right]. \tag{12}$$

The mean elongation is $\langle\rho(t)\rangle = (t/\tau_a)^{\mu+\nu}$ and thus $\alpha = \mu + \nu$. The parameters of Eq. (11), measured from the computed Lagrangian elongations, are $\mu = 0.7$ and

$\nu = 0.1$ for $\sigma^2_{\ln K} = 1$ and $\mu = 1.1$ and $\nu = 0.15$ for $\sigma^2_{\ln K} = 4$.

From the Lagrangian elongation in (12), we compute τ from (3), which integrates ρ^2. Since the mean squared elongation increases in time as $\langle \rho^2 \rangle = (t/\tau_a)^{2\mu+4\nu}$, we approximate (3) by [28]

$$\tau \approx \frac{D\rho^2 t}{s_0^2(1 + 2\mu + 4\nu)}, \tag{13}$$

from which we obtain a simple relationship between the maximum concentration in the lamella in (4) and its current elongation

$$\theta(\rho) \approx \frac{c_0}{\sqrt{1 + \frac{4D\rho^2 t}{s_0^2(1+2\mu+4\nu)}}}. \tag{14}$$

The overall concentration distribution of the distorted lines is thus

$$p_c(c, t) = \int_{\rho(c_0)}^{\rho(c)} d\rho \, \frac{p_\rho(\rho, t)}{c\sqrt{f(\epsilon, \rho, t) f(c, \rho, t)}}, \tag{15}$$

with $f(c, \rho, t) = \ln[c/c_0\sqrt{1 + (4D\rho^2 t/s_0^2(1 + 2\mu + 4\nu))}]$, and $\rho(c)$ is obtained from (14).

The predictions of (15), which is parametrized by the measured elongation rate distribution parameters μ and ν only, are in good agreement with the numerical simulations for all cases where stretched lamellae constitutive of the line do not overlap, i.e., at early times or high Péclet numbers [Fig. 3(a)]. The comparison with the prediction of a purely diffusive model [inset of Fig. 3(a)] shows that flow heterogeneity accelerates considerably the temporal decay of concentration levels through stretching enhanced diffusive mixing. The small concentration asymptotic behavior of the concentration PDF is $p_c \propto 1/[c\sqrt{\ln(1/c)}]$, which is a characteristic of the Gaussian concentration profiles across each lamella as given in (5). The PDF of large concentrations is controlled by the PDF of maximum lamella concentrations $p_m(\theta)$. After the mixing time for $\tau \gg 1$, the maximum lamella concentration θ can be approximated as $\theta \approx s_0/(2\rho\sqrt{Dt})$, as seen from (13) and (14). Since the elongation distribution is log-normal, the PDF of the maximum concentration is also approximately log-normal. Thus, we obtain for the temporal scalings of the moments of θ in this regime $\langle \theta \rangle \propto t^{-\mu+\nu-1/2}$ and $\langle \theta^2 \rangle \propto t^{-2\mu+4\nu-1}$, reflecting those of the mean $\langle c \rangle$ and mean squared $\langle c^2 \rangle$ concentrations.

Interactions between lamellae are enforced at later times and for smaller Péclet numbers, since the average elongation $\langle \rho \rangle \propto t^\alpha$ grows faster than the longitudinal size of the dispersion area $\sigma \propto t^{\alpha/D_f}$ in which the line is confined [remember $D_f \geq 1$ as seen in (10)]. In this regime, the concentration field is composed of bundles of aggregated lamellae separated by regions of low concentration [Fig. 1(c)]. Each

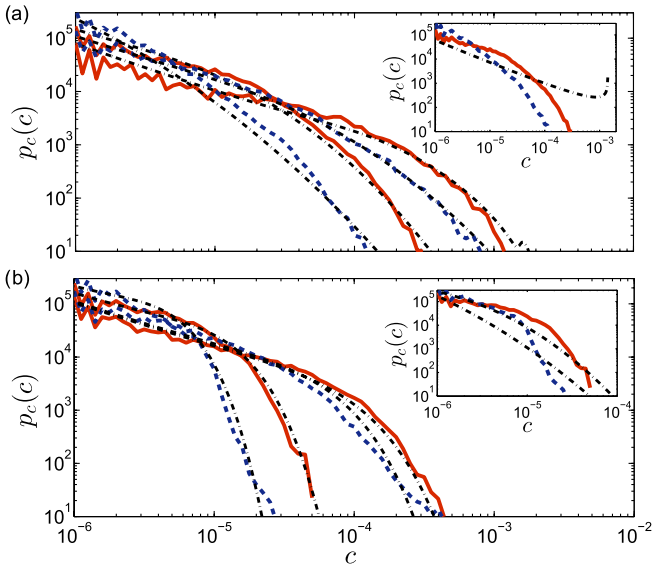

FIG. 3 (color online). (a) Simulated and predicted concentration PDFs in the stretching enhanced diffusion regime (15) for Pe $= 8 \times 10^4$, at times $t_1 = 12.5\tau_a$ and $t_2 = 112.5\tau_a$ and for $\sigma^2_{\ln K} = 1$ (continuous red lines) and $\sigma^2_{\ln K} = 4$ (dashed blue lines). The concentration PDFs are computed over the whole concentration field. The model predictions are shown as dash-dotted black lines. The inset shows the prediction of a purely diffusive model [Eq. (5), with $\theta = c_0/\sqrt{4\pi D t}$] at time t_2. (b) Simulated and predicted concentration PDFs in the lamella interaction regime (17) for Pe $= 8 \times 10^2$, for the same times and log-conductivity variances. The inset shows the predictions of Eq. (15), which does not account for the coalescence process, at time t_2.

bundle contains, on average, n elementary lamellae. When the overlap of the lamellae in the bundles is made at random, the distribution of the maximal concentration c_m in the bundles follows a Gamma distribution [6,23]

$$p_m(c_m, t) = \frac{c_m^{n-1}}{\langle \theta \rangle^n \Gamma(n)} \exp(-c_m/\langle \theta \rangle), \tag{16}$$

where $\langle \theta \rangle$ is the average concentration of the elementary lamellae at time t. Approximating the concentration profile in each aggregate by a Gaussian spatial profile, the concentration PDF conditioned to c_m is $p_c(c|c_m)$, given by (5). Thus, the global concentration PDF in this interaction regime is

$$p_c(c, t) = \int_c^{c_0} dc_m \frac{c_m^{n-1}}{\langle \theta \rangle^n \Gamma(n)} \frac{\exp(-c_m/\langle \theta \rangle)}{c\sqrt{\ln(c_m/\epsilon)\ln(c_m/c)}} \tag{17}$$

for $c \geq \epsilon$. This expression is parametrized by the average number n of lamellae in the bundles and by the average maximum lamella concentration $\langle \theta \rangle \propto t^{-\mu+\nu-1/2}$.

The number n of lamellae with concentration $\langle \theta \rangle$ having coalesced in the bundles is such that it restores, by addition, the average mixture concentration $\langle c \rangle$ so that $n = \langle c \rangle / \langle \theta \rangle$. The number of overlaps simply results from the geometry of the distorted line support: The net length of the line contour within a disk of radius r is r^{D_2}, and it is

composed of $n(r) \propto r^{D_2}/r$ line elements (or segment pairs); D_2 is the the correlation dimension [29], which here is $D_2 \approx D_f$. The radius r is the distance below which two adjacent lamellae are liable to overlap, that is, to merge by diffusion. After the mixing time, the diffusive profile of a single lamella increases like $\sqrt{Dt}$, which sets r. Thus,

$$n = (t/\tau_D)^{(D_f-1)/2}, \tag{18}$$

with $\tau_D = \lambda^2/D$ the diffusion time, setting also the characteristic time for transition to lamella coalescence [21].

The predictions of Eq. (17) are in good agreement with the numerical simulations in the coalescence regime at times $t > \tau_D$ [Fig. 3(b)]. In particular, the large concentration behavior is an exponential decay $p_c \propto \exp(-c/\langle\theta\rangle)$. This property, which is not observed in the first regime when the line does not interact with itself, is a characteristic of the coalescence process described by (16). The low concentration behavior $p_c(c) \propto 1/[c\sqrt{\ln(1/c)}]$ results from the diffusive profiles around the lamella aggregates. The comparison with the prediction of (15) [see the inset of Fig. 3(b)], which does not account for the lamella interactions, shows that the coalescence process tends to increase the intermediate concentration probabilities and to reduce the probability of high and low concentration levels. The temporal scaling of the concentration moments in this regime is $\langle c\rangle = n\langle\theta\rangle \propto t^{-\mu+\nu+D_f/2-1}$ and $\langle c^2\rangle = n(n-1)\times\langle\theta\rangle^2 + n\langle\theta^2\rangle = n(n+1)\langle\theta\rangle^2 \propto t^{-2\mu+2\nu+D_f-2}$ [23].

To conclude, we have offered from first principles a unified framework for mixing in heterogeneous media. The concentration distribution from a uniform line initially tagged in the medium reflects the stretching histories of the line elements as they travel through the medium, and, at some point, the interaction between the line elements dominates the construction mechanism of the concentration field. The approach can be readily extended to 3D by considering 2D sheets as elementary structures rather than 1D material lines, as is done here. This description covers the range of all possible levels of structural heterogeneities and Péclet numbers, thus embracing the rich diversity of mixing behaviors in natural media.

The financial support of the European Commission through FP7 ITN IMVUL (Grant No. 212298) is gratefully acknowledged. Numerical simulations were performed with the software platform H20LAB [30]. M. D. acknowledges the support of the FP7 EU project PANACEA (Grant No. 282900), and the Spanish Ministry of Economy and Competitivity through the project HEART (CGL2010-18450).

*tanguy.le-borgne@univ-rennes1.fr
†Also at Institut Universitaire de France, 75005 Paris, France.

[1] Z. Neufeld and E. Hernandez-Garcia, *Chemical and Biological Processes in Fluid Flows: A Dynamical Systems Approach* (Imperial College, London, 2009).
[2] M. Vergassola, E. Villermaux, and B. I. Shraiman, Nature (London) **445**, 406 (2007).
[3] R. Stocker, Science **338**, 628 (2012).
[4] E. Gouillart, N. Kuncio, O. Dauchot, B. Dubrulle, S. Roux, and J.-L. Thiffeault, Phys. Rev. Lett. **99**, 114501 (2007).
[5] G. Falkovich, K. Gawedzki, and M. Vergassola, Rev. Mod. Phys. **73**, 913 (2001).
[6] E. Villermaux and J. Duplat, Phys. Rev. Lett. **91**, 184501 (2003).
[7] N. Kleinfelter, M. Moroni, and J. H. Cushman, Phys. Rev. E **72**, 056306 (2005).
[8] F. De Barros, M. Dentz, J. Koch, and W. Nowak, Geophys. Res. Lett. **39**, L08404 (2012).
[9] B. Bijeljic, P. Mostaghimi, and M. J. Blunt, Phys. Rev. Lett. **107**, 204502 (2011).
[10] T. Le Borgne, M. Dentz, and J. Carrera, Phys. Rev. Lett. **101**, 090601 (2008).
[11] J. D. Seymour, J. P. Gage, S. L. Codd, and R. Gerlach, Phys. Rev. Lett. **93**, 198103 (2004).
[12] A. M. Tartakovsky, D. M. Tartakovsky, and P. Meakin, Phys. Rev. Lett. **101**, 044502 (2008).
[13] M. Dentz, T. LeBorgne, A. Englert, and B. Bijeljic, J. Contam. Hydrol. **120–121**, 1 (2011).
[14] B. Jha, L. Cueto-Felgueroso, and R. Juanes, Phys. Rev. Lett. **106**, 194502 (2011).
[15] M. Sahimi, *Flow and Transport in Porous Media and Fractured Rock* (Wiley-VCH, Weinheim, 2011).
[16] C. M. Gramling, C. F. Harvey, and L. C. Meigs, Environ. Sci. Technol. **36**, 2508 (2002).
[17] P. Meunier and E. Villermaux, J. Fluid Mech. **476**, 213 (2003).
[18] M. Dentz and D. M. Tartakovsky, Geophys. Res. Lett. **37**, L24406 (2010).
[19] A. Bellin, G. Severino, and A. Fiori, Water Resour. Res. **47**, W01514 (2011).
[20] J. Duplat, A. Jouary, and E. Villermaux, Phys. Rev. Lett. **105**, 034504 (2010).
[21] E. Villermaux, C.R. Mécanique **340**, 933 (2012).
[22] J. Ottino, *The Kinematics of Mixing: Stretching, Chaos, and Transport* (Cambridge University Press, Cambridge, England, 1989).
[23] J. Duplat and E. Villermaux, J. Fluid Mech. **617**, 51 (2008).
[24] W. E. Ranz, AIChE J. **25**, 41 (1979).
[25] P. Meunier and E. Villermaux, J. Fluid Mech. **662**, 134 (2010).
[26] T. Le Borgne, M. Dentz, P. Davy, D. Bolster, J. Carrera, J. R. de Dreuzy, and O. Bour, Phys. Rev. E **84**, 015301 (2011).
[27] H. Risken, *The Fokker-Planck Equation* (Springer, New York, 1996).
[28] J. Duplat, C. Innocenti, and E. Villermaux, Phys. Fluids **22**, 035104 (2010).
[29] P. Grassberger and I. Procaccia, Phys. Rev. Lett. **50**, 346 (1983).
[30] http://h2olab.inria.fr/.